Precise study of hyperfine structure in the $2\,^3P$ state of ^{3}He

J. D. Prestage,* C. E. Johnson,† and E. A. Hinds
J. W. Gibbs Laboratory, Yale University, New Haven, Connecticut 06520

F. M. J. Pichanick
University of Massachusetts, Amherst, Massachusetts 01003
(Received 20 May 1985)

The optical-microwave atomic-beam magnetic resonance technique has been used to measure four hyperfine transitions in the $2\,^3P$ state of ^{3}He. These were used to determine the three hyperfine interaction constants (in MHz) as follows: contact, $C=-4283.84^{+0.02}_{-0.01}$; nuclear-moment-electron-orbit, $D=-28.06\pm0.06$; nuclear-moment-electron-moment, $E=+7.10\pm0.02$. The results, which are in excellent agreement with theory, give a clear indication of the effects of core polarization on the hyperfine structure. We conclude that to the accuracy indicated the structure of the $2\,^3P$ state, including mass-dependent and quantum electrodynamic corrections to the fine structure, and relativistic and core-polarization corrections to the hyperfine structure, is well understood.

I. INTRODUCTION

The spectra of excited states $(1s,nl)$ of ^{3}He have been the subject of several recent experimental investigations. The techniques used have included level crossings,[1] antilevel crossings,[2] various forms of Doppler-free laser spectroscopy,[3,4] and quantum beats in beam-foil spectra.[5]

In this paper we provide details of an optical-microwave atomic-beam experiment on the $2\,^3P$ state. Our results, complemented by those of a level-crossing experiment[1] performed at the University of Michigan in 1967, constitute the most accurate and complete set of data on this state. In a future paper[6] we present an analysis of that experiment based on our comprehensive theory[7] of the $2\,^3P$ state of ^{3}He. The overall results indicate that the structure of the $2\,^3P$ state is now understood to about 20 kHz in the energy-level separations, an improvement of 2—3 orders of magnitude. In particular, for the $2\,^3P$ state we now have an accurate measurement of the p-electron contribution to the hyperfine structure, which was barely resolved from the noise in earlier work,[4] and we have measured previously undetected core-polarization effects.

The basic experimental technique has been described in earlier work on ^{4}He performed at Yale,[8–11] and we give here a brief summary. The overall energy-level scheme of the helium atom is shown in Fig. 1, emphasizing the energy levels of interest and the roles they play in the experiment. Metastable $2\,^3S_1$ atoms are produced by electron bombardment of $1\,^1S_0$ ground-state atoms by passing a beam through an electron gun. The trajectories of the $2\,^3S_1$ beam are shown in Fig. 2. Atoms with $m_S=+1$ and $m_S=-1$ are deflected in opposite directions when passing through each of the inhomogeneous magnets A and B. Atoms with $m_S=0$ are undeflected. In the central region some atoms are caused to transfer to a different m_S sublevel. This is achieved by a combination of (i) optical excitation and decay involving the $2\,^3P$ state, and (ii) magnetic resonance between two sublevels of the $2\,^3P$ state. The placement of the collimator, beam-stops, and detector enables us to select a beam trajectory with initial $m_S=0$, and final $m_S=+1$ or -1. Figure 2 illustrates the arrangement for detection of $m_S=0\rightarrow+1$. This enabled us to measure magnetic dipole resonances within the $2\,^3P$ state as described in Sec. II B. A preliminary report of our results has been published.[12]

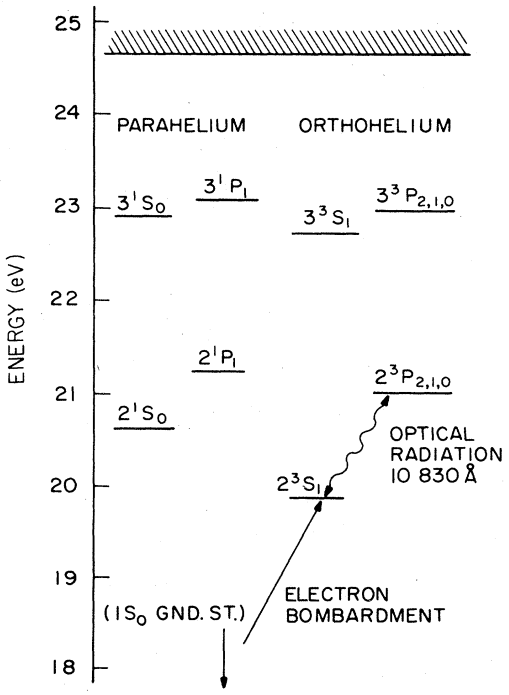

FIG. 1. Energy levels of helium emphasizing those of interest.

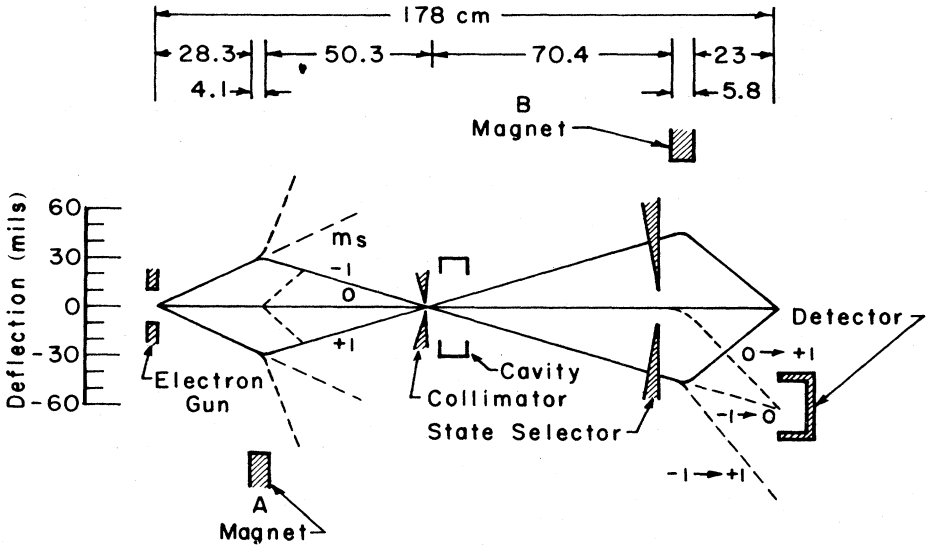

FIG. 2. Diagrammatic top view of the He atomic trajectories.

II. THEORY

A. Energy levels

The structure of the $2\,^3P$ multiplet is shown in Fig. 3 for both ^{3}He and ^{4}He. In ^{3}He the total electronic angular momentum J is not even approximately a good quantum number, because the fine and hyperfine interactions are of comparable strength. Instead, the label J indicates the pure J state of largest overlap. The ^{4}He intervals are taken from Ref. 11 while those of ^{3}He were derived from the experiments described in this paper. The theoretical framework for that derivation has been discussed in some detail in Ref. 7 and will be outlined only briefly here.

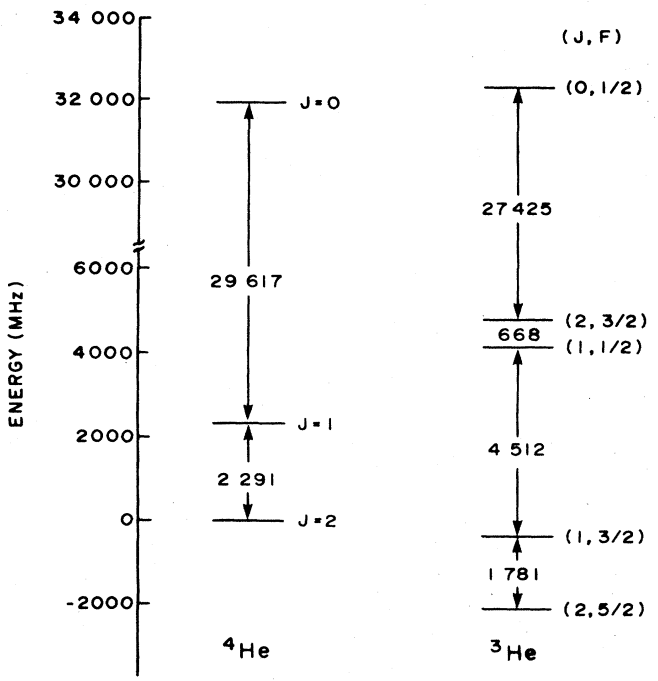

FIG. 3. Comparison of level structures for the $2\,^3P$ states of ^{4}He and ^{3}He.

For the fine-structure interaction in ^{3}He we took the measured ^{4}He splittings and scaled them to account for the various mass-dependent effects. This yielded the effective Hamiltonian given in Table I.

For the hyperfine interaction we took the phenomenological form

$$H_{\rm hfs}=C\mathbf{I}\cdot\mathbf{S}+C'\mathbf{I}\cdot\mathbf{K}+D\mathbf{I}\cdot\mathbf{L}+2\sqrt{10}E\mathbf{I}\cdot\{\mathbf{S}C^{(2)}\}^{(1)}\,, \tag{1}$$

where $\mathbf{I}$ is the nuclear spin, $\mathbf{S}$ and $\mathbf{L}$ are the total electron spin and orbital angular momentum, and $\mathbf{K}$ is the antisymmetric spin operator $\mathbf{s}_1-\mathbf{s}_2$. $C^{(2)}$ is the tensor $(4\pi/5)^{1/2}[Y^{(2)}(\theta_1,\phi_1)+Y^{(2)}(\theta_2,\phi_2)]$ and the curly brackets indicate the contraction of $\mathbf{S}$ with $C^{(2)}$ to form a vector. Justification for using this form is given in Ref. 7. The principal purpose of the experiments described here was to determine the hyperfine coupling constants C, D, and E which can be associated with the contact interaction, the interaction of nuclear moment with electron orbit, and that of nuclear moment with electron spin moment, respectively. The hyperfine Hamiltonian is given in Table II in the $|IM_I\rangle\,|SM_S\rangle\,|LM_L\rangle$ representation.

TABLE I. Effective fine-structure Hamiltonian for ^{3}He in the pure spin representation $|(SL)J\rangle$. The values of the parameters are $\Delta=6.1431\times10^7$ MHz, $E_0=31\,908.742(23)$ MHz, $E_1'=2296.898(9)$ MHz, $E_2=0$, $E_M=-17.037$ MHz.

	$2\,^1P_1$	$2\,^3P_0$	$2\,^3P_1$	$2\,^3P_2$
$2\,^1P_1$	Δ		E_M	
$2\,^3P_0$		E_0		
$2\,^3P_1$	E_M		E_1'	
$2\,^3P_2$				E_2

The experiments were done in a static magnetic field and therefore a Zeeman Hamiltonian was required for the interpretation of our data. We took the simple form

$$H_Z=\mu_B(g_L'\mathbf{L}+g_S'\mathbf{S}+g_I'\mathbf{I})\cdot\mathbf{B}\ , \tag{2}$$

in which μ_B is the Bohr magneton[13] 1.399 613 7(3) MHz/G, g_L' and g_S' are the $2\,^3P$ orbital and spin g factors, and g_I' is the ^{3}He nuclear-spin g factor,[14] $2.317\,482\,3(7)\times10^{-3}$. Our value of g_S' was 2.002 243 2(24) which we took from the ^{4}He measurement by S. Lewis *et al.*[9] Since the largest mass-dependent contribution to g_S' is of order $\alpha m/M$ no isotope correction was needed for our purposes. The appropriate value of g_L' was derived rather indirectly. According to a level-crossing measurement by Lhuillier *et al.*,[15] the value of g_L' for ^{4}He is larger than the simple lowest-order value $g_L=(1-m/M)$ by $(4.9\pm2.9)\times10^{-6}$. Also, Lewis and Hughes[16] have computed that the mass-independent correction to g_L is -8.3×10^{-6}. We therefore took the mass-dependent part of g_L' to be $(13.2\pm2.9)\times10^{-6}$ in ^{4}He and hence $(9.3\pm2.4)\times10^{-6}$ in ^{3}He, giving $g_L'=0.999\,826\,5(24)$ in ^{3}He. This value was subsequently

TABLE II. Effective Hamiltonian for the $2\,^3P$ states of ^{3}He including $2\,^1P$ interactions. Values of the fine-structure parameters Δ, E_0, E_1', and E_M are given in Table I. Hyperfine parameters C, C', D, and E are discussed in the text and ϵ is an abbreviation for $E/5$.

				2^1P			2^3P								
	M_I			$\frac{1}{2}$	$-\frac{1}{2}$	$\frac{1}{2}$	$\frac{1}{2}$	$-\frac{1}{2}$	$\frac{1}{2}$	$\frac{1}{2}$	$-\frac{1}{2}$	$-\frac{1}{2}$	$\frac{1}{2}$	$\frac{1}{2}$	$\frac{1}{2}$
		M_S		0	0	0	1	1	1	0	1	0	1	0	-1
			M_L	1	1	0	1	1	0	1	0	1	-1	0	1
2^1P	$\frac{1}{2}$	0	1	$\Delta+\frac{D}{2}$				$\frac{-C'}{\sqrt{2}}-\sqrt{2}\epsilon$	$\frac{-E_M}{\sqrt{2}}+3\epsilon$	$\frac{E_M}{\sqrt{2}}+\frac{C'}{2}-2\epsilon$					
	$-\frac{1}{2}$	0	1		$\Delta-\frac{D}{2}$	$\frac{D}{\sqrt{2}}$					$\frac{-E_M}{\sqrt{2}}-3\epsilon$	$\frac{E_M}{\sqrt{2}}-\frac{C'}{2}+2\epsilon$	$6\sqrt{2}\epsilon$	$-3\sqrt{2}\epsilon$	$\frac{C'}{\sqrt{2}}+\sqrt{2}\epsilon$
	$\frac{1}{2}$	0	0		$\frac{D}{\sqrt{2}}$	Δ					$\frac{-C'}{\sqrt{2}}+\sqrt{8}\epsilon$	$-3\sqrt{2}\epsilon$	$\frac{-E_M}{\sqrt{2}}-3\epsilon$	$\frac{C'}{2}+4\epsilon$	$\frac{E_M}{\sqrt{2}}-3\epsilon$
2^3P	$\frac{1}{2}$	1	1				$\frac{C}{2}+\frac{D}{2}+2\epsilon$								
	$-\frac{1}{2}$	1	1	$\frac{-C'}{\sqrt{2}}-\sqrt{2}\epsilon$				$\frac{-C}{2}-\frac{D}{2}-2\epsilon$	$\frac{D}{\sqrt{2}}+3\sqrt{2}\epsilon$	$\frac{C}{\sqrt{2}}-\sqrt{2}\epsilon$					
	$\frac{1}{2}$	1	0	$\frac{-E_M}{\sqrt{2}}+3\epsilon$				$\frac{D}{\sqrt{2}}+3\sqrt{2}\epsilon$	$\frac{E_1'}{2}+\frac{C}{2}-4\epsilon$	$\frac{-E_1'}{2}+3\epsilon$					
	$\frac{1}{2}$	0	1	$\frac{E_M}{\sqrt{2}}+\frac{C'}{2}-2\epsilon$				$\frac{C}{\sqrt{2}}-\sqrt{2}\epsilon$	$\frac{-E_1'}{2}+3\epsilon$	$\frac{E_1'}{2}+\frac{D}{2}$					
	$-\frac{1}{2}$	1	0		$\frac{-E_M}{\sqrt{2}}-3\epsilon$	$\frac{-C'}{\sqrt{2}}\sqrt{8}\epsilon$					$\frac{E_1'}{2}-\frac{C}{2}+4\epsilon$	$\frac{-E_1'}{2}-3\epsilon$	$\frac{D}{\sqrt{2}}-3\sqrt{2}\epsilon$	$\frac{C}{\sqrt{2}}+2\sqrt{2}\epsilon$	0
	$-\frac{1}{2}$	0	1		$\frac{E_M}{\sqrt{2}}-\frac{C'}{2}+2\epsilon$	$-3\sqrt{2}\epsilon$					$\frac{-E_1'}{2}-3\epsilon$	$\frac{E_1'}{2}-\frac{D}{2}$	$6\sqrt{2}\epsilon$	$\frac{D}{\sqrt{2}}$	$\frac{C}{\sqrt{2}}-\sqrt{2}\epsilon$
	$\frac{1}{2}$	1	-1		$6\sqrt{2}\epsilon$	$\frac{-E_M}{\sqrt{2}}-3\epsilon$					$\frac{D}{\sqrt{2}}-3\sqrt{2}\epsilon$	$6\sqrt{2}\epsilon$	$\frac{E_0}{3}+\frac{E_1'}{2}+\frac{C}{2}-\frac{D}{2}+2\epsilon$	$\frac{-E_0}{3}-3\epsilon$	$\frac{E_0}{3}-\frac{E_1'}{2}$
	$\frac{1}{2}$	0	0		$-3\sqrt{2}\epsilon$	$\frac{C'}{2}+4\epsilon$					$\frac{C}{\sqrt{2}}+2\sqrt{2}\epsilon$	$\frac{D}{\sqrt{2}}$	$\frac{-E_0}{3}-3\epsilon$	$\frac{E_0}{3}$	$\frac{-E_0}{3}+3\epsilon$
	$\frac{1}{2}$	-1	1		$\frac{C'}{\sqrt{2}}+\sqrt{2}\epsilon$	$\frac{E_M}{\sqrt{2}}-3\epsilon$					0	$\frac{C}{\sqrt{2}}-\sqrt{2}\epsilon$	$\frac{E_0}{3}-\frac{E_1'}{2}$	$\frac{-E_0}{3}+3\epsilon$	$\frac{E_0}{3}+\frac{E_1'}{2}-\frac{C}{2}+\frac{D}{2}-2\epsilon$

justified by our fit to the ^{3}He level-crossing data of German and Sands[1] which yielded $g_L'=0.999\,828\,6(20)$. (In fact, either value is far more accurate than we require for the present analysis of hyperfine parameters.) The purely relativistic g factor[9] g_x was small enough to neglect, as was the quadratic Zeeman interaction.[9] The $2\,^3P$ Zeeman sublevels of ^{3}He are plotted in Fig. 4 which also shows the four transitions studied in our experiments.

The magnetic field in the resonance region was calibrated by means of Zeeman transitions in the $2\,^3S$ state. The levels, labeled 1—6 for convenience, are shown in Fig. 5 and their eigenvalues $W(F,m_F)$ are given by

$$W(\tfrac{3}{2},\pm\tfrac{3}{2})=\pm(g_J+g_I/2)\mu_B B\ , \tag{3}$$

$$W(F,\pm\tfrac{1}{2})=E/2\pm(g_J/2)\mu_B B +(-1)^{F-1/2}[E^2\pm\tfrac{2}{3}E(g_J-g_I)\mu_B B +(g_J-g_I)^2(\mu_B B)^2]^{1/2}\ .$$

The constants not already defined are (from Refs. 17 and 18, respectively)

$$E=6739.701\,177(16)\ ,$$

$$g_J=2.002\,237\,38(14)\ .$$

In a weak magnetic field the energy levels are characterized by the quantum numbers (F,M_F), and in a strong field by (M_S,M_I). While passing through the deflecting magnets (A and B in Fig. 2) the strong-field regime of Fig. 5 is reached, and the trajectories are determined by M_S as illustrated in Fig. 2.

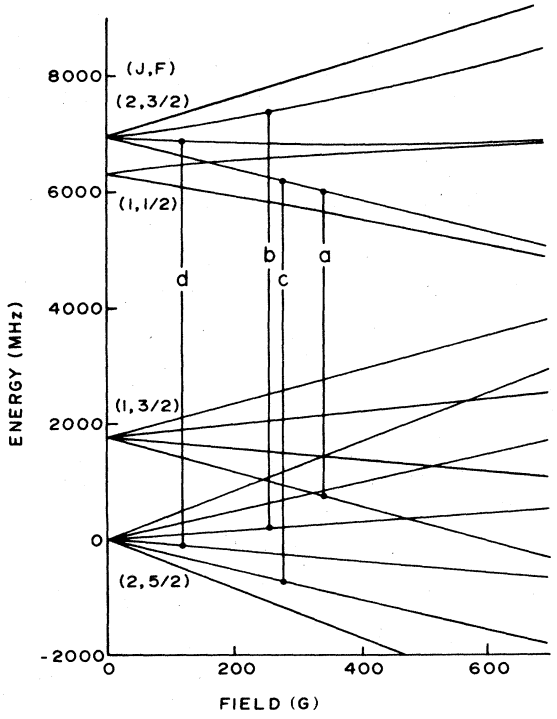

FIG. 4. Energy levels of the $2\,^3P$ state of ^{3}He as a function of magnetic field. Transitions measured in this work are indicated. The $J=0$, $F=\frac{1}{2}$ level has been omitted.

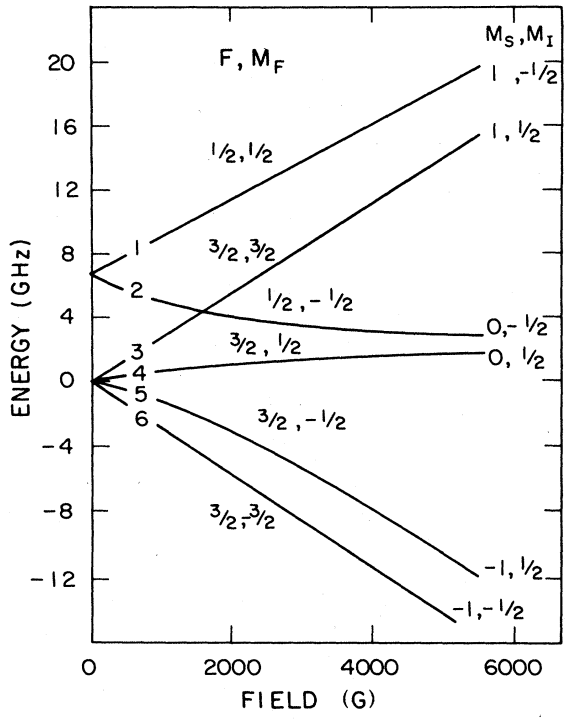

FIG. 5. Energy levels of the $2\,^3S_1$ state of ^{3}He as a function of magnetic field. In weak fields the quantum numbers (F,M_F) are used while in strong fields the numbers (M_S,M_I) are appropriate. Sublevels have been labeled 1—6 for convenience in the text.

B. Line shape and signal strength

When the beam is optically excited to the $2\,^3P$ state and then decays, the atoms transferred from $2\,^3S_1$ ($M_s=0$) to either $2\,^3S_1$ ($M_s=+1$) or $2\,^3S_1$ ($M_S=-1$) are observed as a "light-flop signal," $L_{0\to\pm1}$, because of the change in their trajectory. The positions of the beam stops and detector are illustrated in Fig. 2 for the case of the $M_S(0\to+1)$ light flop. Note from Fig. 5 that the three pairs of levels (1,3), (2,4), and (5,6) have $M_S=+1$, 0, and -1, respectively. The light-flop probability is[8]

$$L_{0\to\pm1}=\sum_{i,f,p}\sigma_{ip}\gamma_{pf}\ , \tag{4}$$

where σ and γ are, respectively, the $2\,^3S\to2\,^3P$ excitation and $2\,^3P\to2\,^3S$ decay probabilities for the particular sublevels denoted by the subscripts. From Fig. 5 we have $i=2,4$ with $f=1,3$ for a $(0\to+1)$ light flop and $f=5,6$ for a $(0\to-1)$ light flop. Each sum is over all the $2\,^3P$ sublevels, denoted by the subscripts p.

The light flop is modified when an oscillating microwave magnetic field induces a dipole transition between two $2\,^3P$ sublevels α and β. We observe this change in the light flop and normalize it to the light flop measured without microwave power. The normalized signal $S^{\alpha\beta}_{0\to\pm1}$ is given by[8]

$$S^{\alpha\beta}_{0\to\pm1}=\frac{\rho(\alpha,\beta)\sum_{i,f}(\sigma_{i\beta}-\sigma_{i\alpha})(\gamma_{\alpha f}-\gamma_{\beta f})}{\sum_{i,f,p}\sigma_{ip}\gamma_{pf}} . \quad (5)$$

The quantity $\rho(\alpha,\beta)$ is the microwave transition probability[8]

$$\rho(\alpha,\beta)=\frac{2\,|\,B_1\mu_B V_{\alpha\beta}/\hbar\,|^2}{(\omega_{\alpha\beta}-\omega_0)^2+4\,|\,B_1\mu_B V_{\alpha\beta}/\hbar\,|^2+\gamma^2} , \quad (6)$$

where μ_B is the Bohr magneton, $2B_1$ is the amplitude of the microwave field, $B_1\mu_B V_{\alpha\beta}$ is the magnetic dipole matrix element, $\omega_{\alpha\beta}$ is the energy separation of α and β in units of angular frequency, ω_0 is the angular frequency of the microwave field, and $\gamma\approx10^7$ s^{-1} is the decay rate of the $2\,^3P$ population.

Experimentally the signal is observed by keeping ω_0 fixed and sweeping the homogeneous magnetic field, giving Eq. (6) a resonant behavior as $\omega_{\alpha\beta}$ changes. The resonance line shape also depends slightly on the implicit field dependence of σ, γ, and $|\,V_{\alpha\beta}\,|^2$.

For small values of B_1 the resonance has a (natural) linewidth in frequency units of $2\gamma/2\pi\approx3.2$ MHz, but the ratio of signal to linewidth is maximized with $2B_1=\sqrt{2}\gamma/\mu_B\,|\,V_{\alpha\beta}\,|\approx2$ G and the broadened linewidth is then given by

$$\Delta\nu=\sqrt{3}\gamma/\pi\approx5\text{ MHz} . \quad (7)$$

The four ^3P transitions observed in this work were, in (J,F,M_F) notation,

(a) $(2,\frac{3}{2},-\frac{3}{2})\leftrightarrow(1,\frac{3}{2},-\frac{3}{2})$,

(b) $(2,\frac{3}{2},\frac{1}{2})\leftrightarrow(2,\frac{5}{2},\frac{1}{2})$,

(c) $(2,\frac{3}{2},-\frac{3}{2})\leftrightarrow(2,\frac{5}{2},-\frac{3}{2})$,

(d) $(2,\frac{3}{2},-\frac{1}{2})\leftrightarrow(2,\frac{5}{2},-\frac{1}{2})$.

Note that these are all $\Delta M_F=0$ transitions which have only second-order field dependence and accordingly require less accuracy in the magnetic field measurement. The calculated signal strengths for optimum microwave field are illustrated in Fig. 6 as functions of magnetic field. Transitions (a), (c), and (d) were observed with the $(0\to-1)$ light-flop trajectory, and transition (b) with the $(0\to+1)$ trajectory. The values of the frequency, magnetic field, and field dependence for each transition are summarized in Table III.

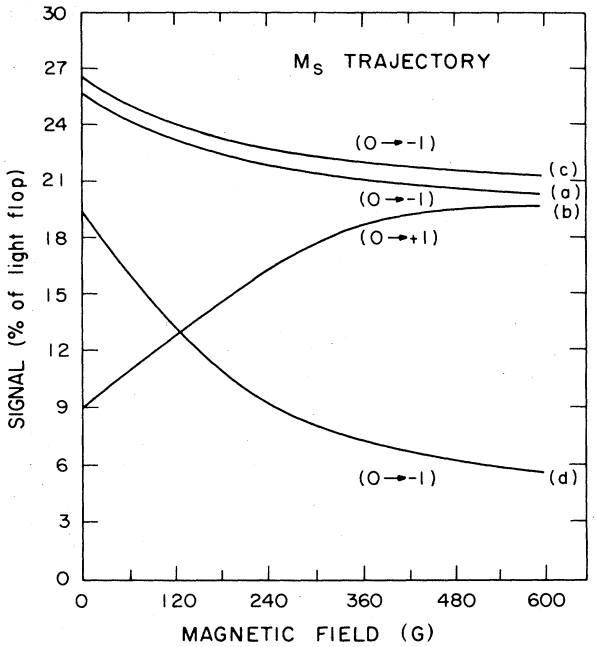

FIG. 6. Calculated signal strengths for the four measured transitions as functions of magnetic field. These were computed assuming the optimum microwave field as defined in the text.

III. APPARATUS

The measurements of transitions (c) and (d) were performed in 1967 on our old apparatus, which has been already described in Ref. 8 except for the microwave system described below. Transitions (a) and (b) were performed on our current apparatus, described in various stages in Refs. 9, 10, and 11 with modifications to the metastable source, and with new field-measurement and microwave systems, also described below. A schematic overview of the apparatus is given in Fig. 7.

A. Metastable $2\,^3S$ source

The source gas was ^{3}He with an isotopic purity of 99.9%, and because of its cost the gas had to be recycled. In order to accomplish this the vacuum system had a forepump with special seals, whose output was fed to a purifying system. This consisted of a simple liquid-

TABLE III. Summary of the microwave frequencies and magnetic fields used for the four transitions. The dependence of transition frequency on magnetic field is given in the last column.

	Transition (JFM_F)	Transition $(J'F'M'_F)$	Frequency (MHz)	Field (G)	$\partial f/\partial B$ (MHz/G)
(a)	$(2,\frac{3}{2},-\frac{3}{2})$	$(1,\frac{3}{2},-\frac{3}{2})$	5209.700	347	0.253
(b)	$(2,\frac{3}{2},\frac{1}{2})$	$(2,\frac{5}{2},\frac{1}{2})$	7159.200	264	1.31
(c)	$(2,\frac{3}{2},-\frac{3}{2})$	$(2,\frac{5}{2},-\frac{3}{2})$	6870.000	280	−0.191
(d)	$(2,\frac{3}{2},-\frac{1}{2})$	$(2,\frac{5}{2},-\frac{1}{2})$	6990.000	164	0.488

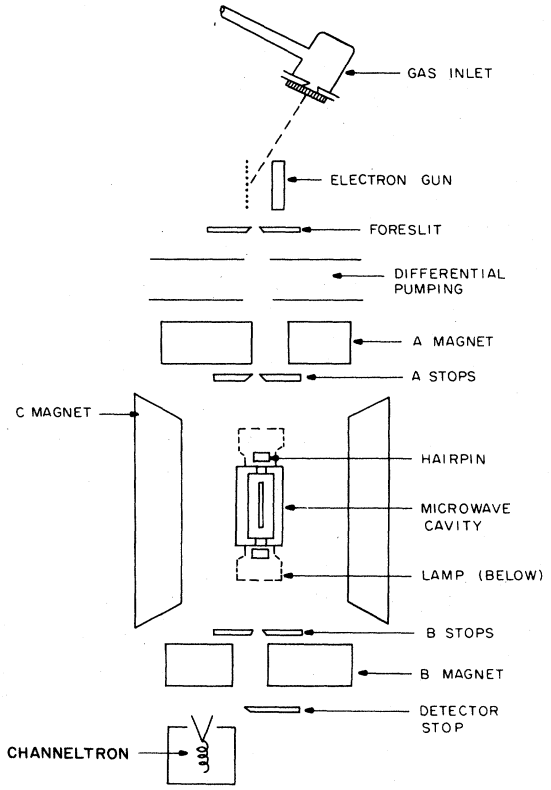

FIG. 7. Schematic top view of the apparatus.

nitrogen trap to remove oil and water vapors followed by a liquid-nitrogen-cooled trap filled with zeolite to absorb other gases. The purified ^{3}He was then returned to the gas-handling system to be fed into the beam. Under normal operating conditions problems with impurities in the beam were not encountered. A booster diffusion pump between the backing line of the main diffusion pumps and the recirculating pump was essential for handling the gas load on the vacuum system.

A top view of the modified source is shown in Fig. 8. A beam of $1\,^1S_0$ ground-state helium atoms, formed by effusion through a multichannel array, passed through an electron gun where excitation to the metastable $2\,^3S_1$ state occurred. There was also excitation to the metastable $2\,^1S_0$ state which has no magnetic moment and was not important in this experiment. The multichannel array, of thickness 1 mm, contained capillaries of diameter 2.4×10^{-2} mm, with a density of about 5×10^4 capillaries/cm^2, and the total area was 1.5 cm by 0.3 cm. The emerging vertical ribbon beam was estimated, following the analysis of Ref. 19, to have a full angular width at half maximum intensity of 2.5°, a peak flux of 5×10^{20} atoms/sec sr, and a total throughput of 2×10^{18} atoms/sec. The electron gun consisted of a solid anode and 16 vertical filaments made of 1% thoriated tungsten, 0.15 mm in diameter and 2.5 cm long. Spacing between the anode and filaments was 1.5 cm, and with 500 V applied between them a typical emission current was 140 mA. The gas source and array were positioned so that the beam entered the gun at an angle as shown in Fig. 8. This was to compensate for atomic recoil after electron excitation, and it was found that a maximum metastable beam rate was obtained with an angle of approximately 12° with respect to the beam line. The gas source was located 10 cm from the gun. We were able to run for several hundred hours before the beam intensity was reduced appreciably through blockage of the capillaries by sputtered tungsten.

In Fig. 9(a) we show the Stern-Gerlach beam profile with only the B magnet (Fig. 2) in operation. The central peak consists of $2\,^3S_1$ ($M_S=0$) atoms, $2\,^1S_0$ atoms, and a small contribution from uv light originating in the source, while the side peaks are the $2\,^3S_1$ ($M_S=\pm1$) atoms. Figure 9(b) shows the beam profile with both deflecting magnets in operation; the deflected atoms have been removed by means of beam stops leaving only the central peak. The new source produced an improvement in intensity of about a factor of 3 for the deflected atoms with better spatial resolution.

B. Microwave systems

All the $2\,^3P$ transitions were excited by passing the atomic beam through rectangular TE_{10n} cavities. A diagram showing the geometry of the arrangement is given in Fig. 10. The number n was even so that the peak microwave field occurred at the center of the cavity where

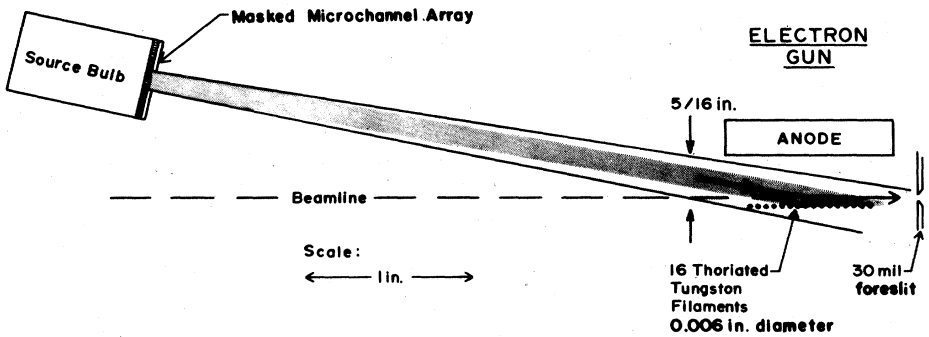

FIG. 8. Top view of the $2\,^3S_1$ metastable source.

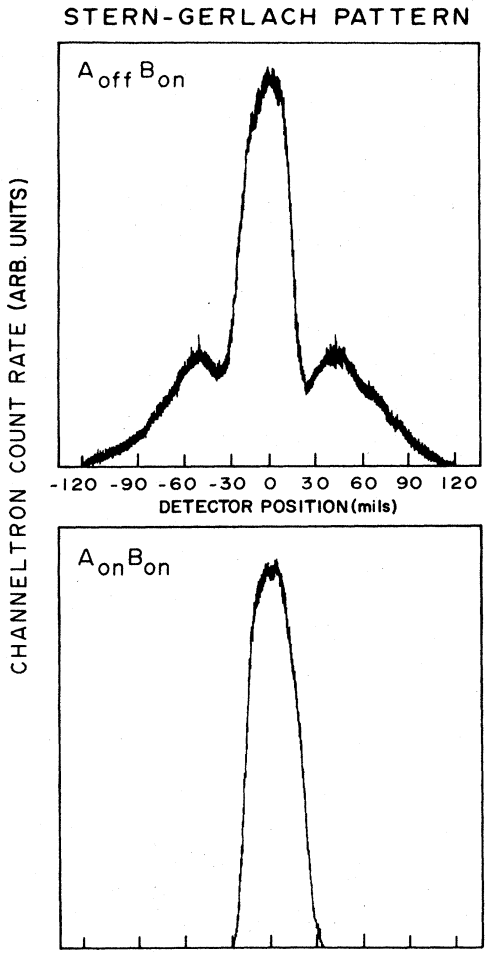

FIG. 9. (a) Stern-Gerlach beam profile with only one deflecting magnet in operation, (b) beam profile with both deflecting magnets in operation.

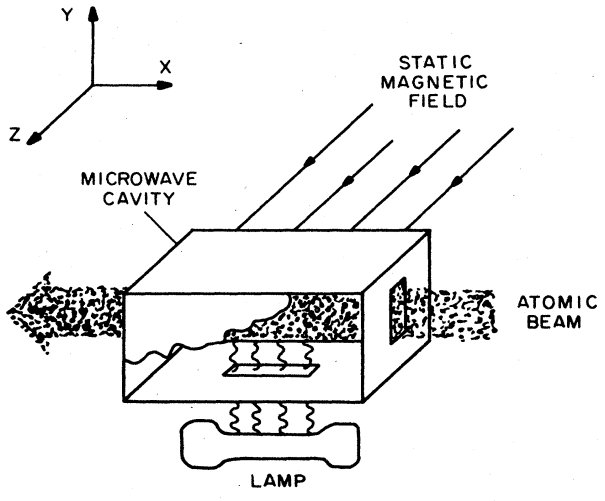

FIG. 10. Geometrical arrangement of atomic beam, light source, microwave cavity, and uniform magnetic field.

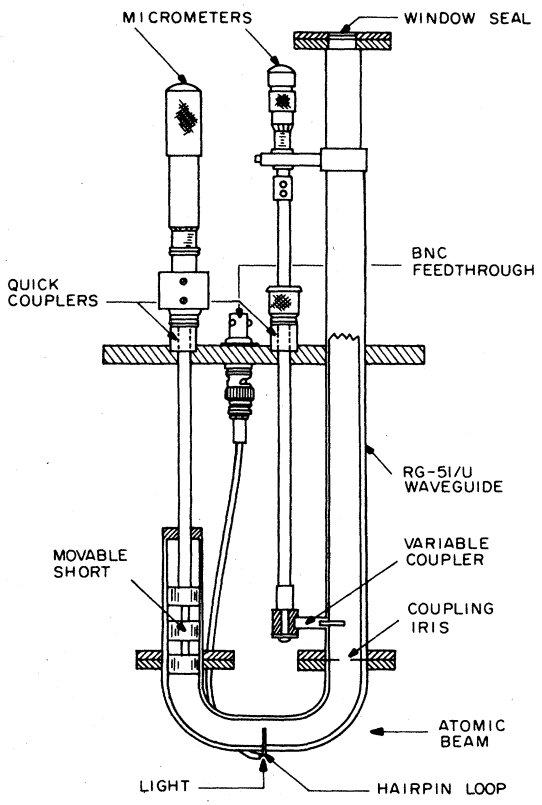

FIG. 11. Microwave cavity used for transitions (c) and (d).

the optical radiation entered vertically from below.

The design used for transitions (c) and (d) is shown in Fig. 11. The cavity consisted of a section of 2.5×1.25 cm waveguide (H band) with two E-plane bends forming a U shape. Microwaves entered the cavity by means of an

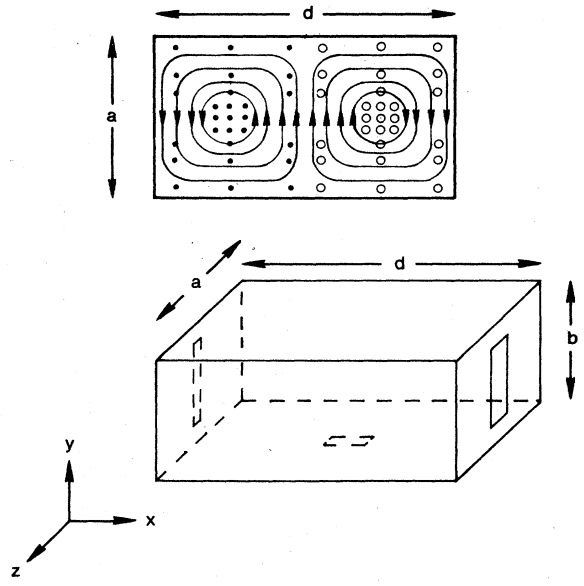

FIG. 12. Schematic diagram of cavity used for transitions (a) and (b) showing the geometry of the microwave fields.

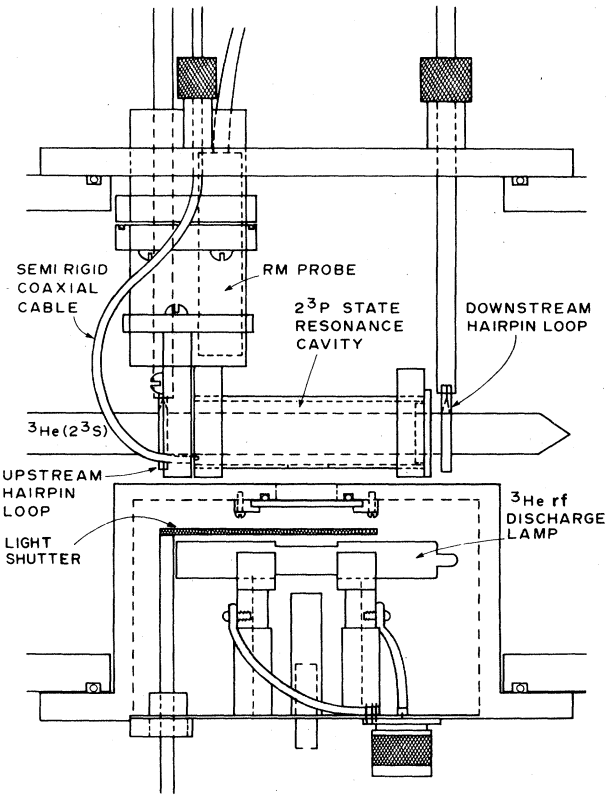

FIG. 13. Mounting arrangement for the cavity used for transitions (a) and (b). The $2\,^3S_1$ hairpins, rubidium magnetometer, and light source are also shown. Light source was modulated by a rotatable shutter.

iris coupling to the input waveguide, and the coupling was adjusted with a movable teflon plug controlled from outside the vacuum via a micrometer feed-through. The microwaves entered the vacuum system through a mica window seal in the input waveguide. The cavity was tuned at the other end using a movable choke short also controllable from outside the vacuum system. A small rf loop was inserted into the cavity through the bottom slit. This enabled us to measure the magnetic field by exciting a $2\,^3S_1$ Zeeman resonance. This cavity was operated in the TE_{104} mode at 7 GHz. It had a Q of 1000 and gave a microwave magnetic field of 2 G with an input power of about 20 W.

The cavities used for transitions (a) and (b) operated in the TE_{102} mode and were of a boxlike construction shown in Fig. 12. The dimensions are shown in the lower part of the diagram together with the slit for the atomic beam (traveling in the x direction) and the optical radiation (entering in the y direction). The uniform static magnetic field was in the z direction. They were made of brass and highly polished on the inside to reflect the optical radiation back on to the beam. The tuning and coupling to the input were optimized prior to mounting in the vacuum system. The characteristics of the two cavities are summarized below.

Transition	Dimensions (cm) a	b	d	Frequency (GHz)	Q
(a)	4.7	2.2	7.3	5.2	3000
(b)	3.5	1.6	5.2	7.2	1500

The entire resonance region assembly is illustrated in Fig. 13. Included in the assembly were two rf hairpin loops

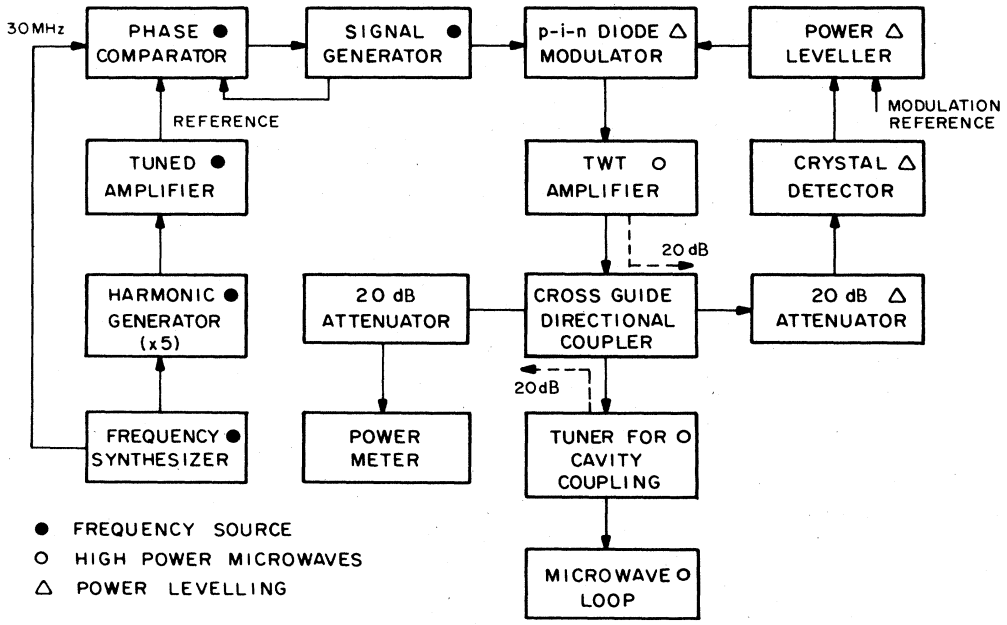

FIG. 14. Block diagram of the microwave system used for transitions (c) and (d).

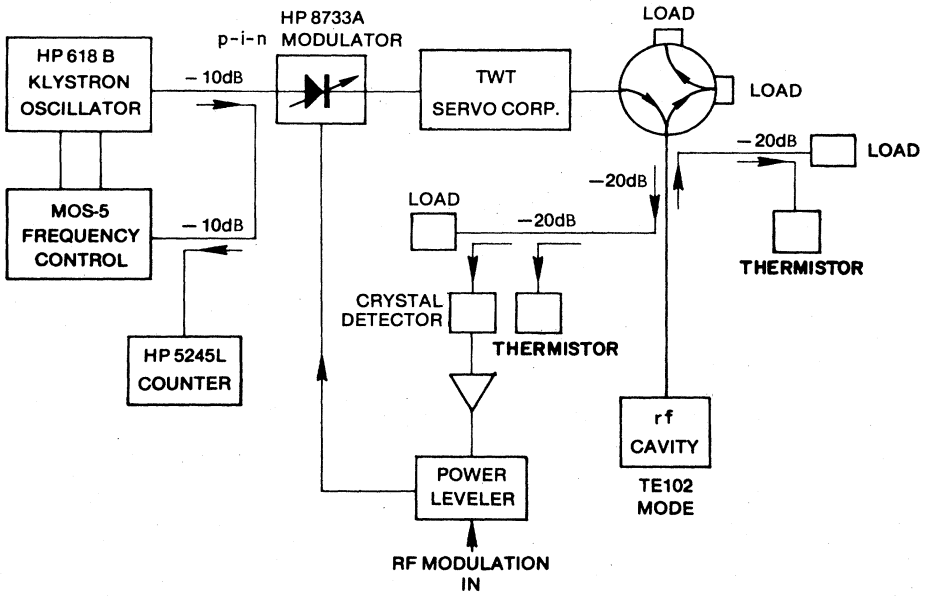

FIG. 15. Block diagram of the microwave system used for transitions (a) and (b).

and a rubidium magnetometer (RM) probe, which are described in Sec. III C. The cavity itself was water-cooled to stabilize its resonant frequency. The mounting of the discharge lamp which provided the optical radiation is shown also. The lamp and shutter were outside the vacuum.

Block diagrams of the microwave systems are given in Fig. 14 for transitions (c) and (d), and in Fig. 15 for transitions (a) and (b). In each case the high-power microwaves were generated by a traveling-wave tube (TWT) amplifier whose input was modulated by a PIN diode. In Fig. 14 the input to the TWT was from a klystron oscillator whose phase was locked to that of a harmonic obtained from a frequency synthesizer. In Fig. 15 the klystron was stabilized using a commercial controller. Other components relate to power leveling and to measurement of frequency, power output, and standing-wave ratio in the line to the cavity.

C. Magnetic field measurement

The system used to calibrate and monitor the magnetic field for transitions (c) and (d) was similar to that used earlier, but a much improved system was used for transitions (a) and (b). During the course of an experimental run the field was set and stabilized using a rubidium magnetometer,[20] the RM probe shown in Fig. 13. The probe was a rubidium vapor cell, optically pumped by circularly polarized light from a rubidium discharge lamp. A feedback loop locked the static magnetic field to the optical pumping resonance signal from the ground-state rf transition $^2S_1$ ($F=2$, $m_F=-2\leftrightarrow-1$). Details of how the magnet current was controlled have been given in Ref. 11. The desired value of the field was set by selecting the rf transition frequency on a frequency synthesizer, setting the magnetic field near the Rb resonance, and then closing the feedback loop.

Since the RM probe was not placed exactly at the location of the $2\,^3P$ resonance, it was necessary periodically to measure the small magnetic field offset between the two. This was done by inducing $2\,^3S_1$ Zeeman transitions using the rf "hairpin" loops labeled as upstream and downstream in Fig. 13. These loops allowed us to observe the Zeeman resonances by the separated oscillating fields technique, giving an accurate measurement of the average magnetic field in the $2\,^3P$ transition region between the loops. Figure 16 shows an example of one of these resonances with the two loops fed in phase. At the same time the field was measured using the RM probe. The difference between the two was typically 20 mG, and was consistent with the known field gradients in the region. In this way we were able to know the absolute magnetic field in the cavity during our $2\,^3P$ measurements with an uncertainty less than 10 mG.

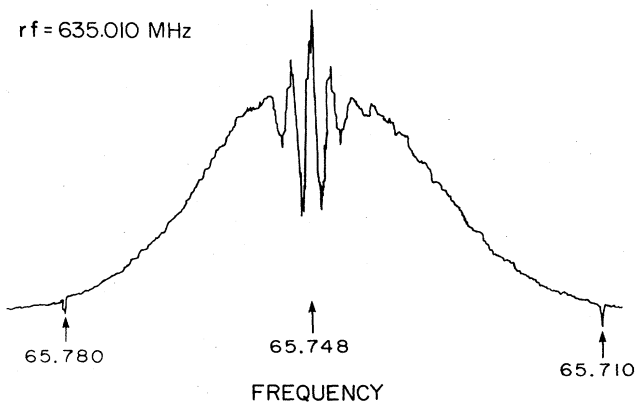

FIG. 16. Typical $2\,^3S_1$ separated oscillating field line shape used for field calibration.

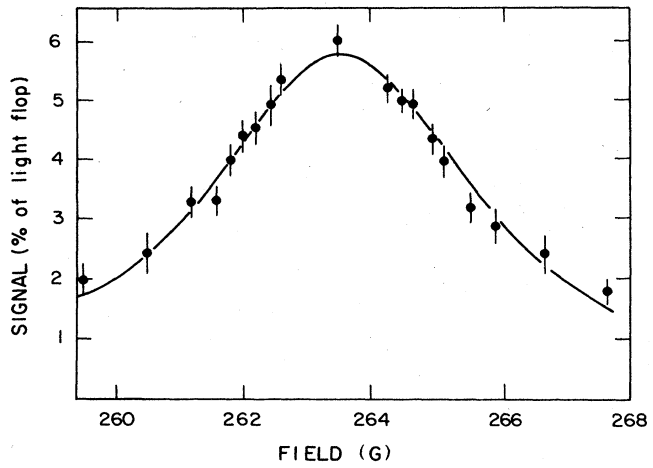

FIG. 17. Typical resonance curve for transition (b).

IV. RESULTS AND DATA ANALYSIS

A. Experimental procedure

A $2\,^3P$ resonance curve was plotted by taking measurements of the signal at various values of the magnetic field with the microwave frequency fixed. About 20 field points were chosen for each measured resonance, and they were taken in symmetric pairs about the center of the line in order to minimize any artificial asymmetries due to drifts in microwave power. Typical resonance curves are shown in Fig. 17 for transition (b) and Fig. 18 for transition (c). The error bars are based on the measured variance of the signal which was found to be consistent with counting statistics. The resonance signal normalized to the light flop [Eq. (5)] was measured as $(N_M-N_L)/(N_L-N_B)$, where N_M were the microwave signal counts (microwaves and light on), N_L were the light flop counts (microwaves off, light on), and N_B were the background counts (microwaves and light off). These counts were made automatically using a computer to modulate the microwaves and light.

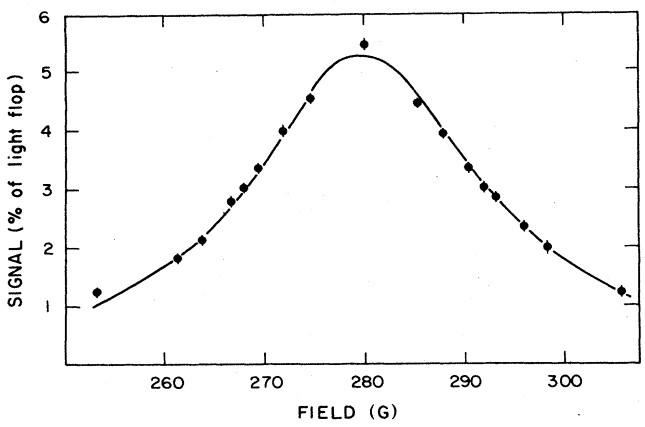

FIG. 18. Typical resonance curve for transition (c).

B. Line-shape fitting

The first step in the fitting procedure was to diagonalize the full fine-hyperfine-Zeeman Hamiltonian for the relevant magnetic field at each data point. This yielded a value for $\omega_{\alpha\beta}$, the energy separation in angular frequency units between the two $2\,^3P$ sublevels, which appears in Eq. (6). The diagonalization procedure required a number of input parameters defined in Sec. II. These were fine structures and Zeeman g factors whose values were computed[7] for ^{3}He from previous experimental work on ^{4}He, and the parameter C', which was not required to high accuracy and was taken from theory.[7] The hyperfine parameters C, D, and E were to be determined from our experiments but could not be obtained as independent fitting parameters from the data of a single transition. Our procedure was temporarily to fix C and E at reasonable values C_0 and E_0 and to use D as a fitting parameter for the data of a particular transition. The line shapes were fitted to Eq. (5), therefore, using the height and width of the resonance and D as the only free parameters. The iterative least-squares-fitting procedure has been described in the earlier papers. Four different values of D were obtained from the weighted means of our runs on each of the four transitions. These were then reconciled by adjusting our initial values for C_0 and E_0 as described below.

C. Data analysis

The line-fitting procedure gave us the value of D for which the resonance frequency $\omega_{\alpha\beta}$ would equal the microwave frequency ω_0. This value we now call D_0 because it depended on the assumed values C_0 and E_0 for the other hyperfine parameters. As pointed out above, C, D, and E are not uniquely determined by a single transition because any set will satisfy the resonance condition provided

$$\delta\omega=\frac{\partial\omega}{\partial C}(C-C_0)+\frac{\partial\omega}{\partial D}(D-D_0)+\frac{\partial\omega}{\partial E}(E-E_0)=0\,, \tag{8}$$

in which $\omega\equiv\omega_{\alpha\beta}$. Equation (8) defines a plane, all points on which give a least-squares fit to the line shape of a particular transition, a linear approximation which is adequate when C_0, D_0, and E_0 are sufficiently close to the "best" values, as was the case. For purposes of analysis we have found it convenient to rewrite the plane as

$$(D-D_0)-\frac{\partial D}{\partial C}(C-C_0)-\frac{\partial D}{\partial E}(E-E_0)=0\,, \tag{9}$$

where

$$\frac{\partial D}{\partial C}=-\frac{\partial f/\partial C}{\partial f/\partial D}$$

and

$$\frac{\partial D}{\partial E}=-\frac{\partial f/\partial E}{\partial f/\partial D}\,.$$

The coefficients $\partial D/\partial C$ and $\partial D/\partial E$ were determined for each transition by diagonalizing the Hamiltonian for

TABLE IV. Equations of the least-squares planes for the four transitions. The hyperfine parameters C, D, and E are defined in the text.

Transition	Equation (MHz)
(a)	$(D+27.440)-3.94(C+4283.80)+5.45(E-6.860)=0$
(b)	$(D+28.390)+2.40(C+4283.70)-0.0845(E-7.098)=0$
(c)	$(D+27.923)+4.87(C+4283.85)+0.978(E-6.981)=0$
(d)	$(D+28.055)+3.51(C+4283.85)+0.462(E-7.014)=0$

several trial values of the parameters. They were different for each of the four transitions, and thus our overall results gave us a set of four intersecting planes, whose equations are summarized in Table IV.

The "true" values of C,D,E define a unique point at which the four planes should intersect. In practice the best values are those which give the closest approach to intersection at a point. This was found by the least-squares method in which one minimizes the quantity

$$\chi^2=\sum_{l=1}^{4}\left[\frac{d_l}{\sigma_l}\right]^2 .$$

The sum is over the four transitions, d_l is the perpendicular distance from a point (C,D,E) to the lth plane, and σ_l is the associated experimental error. The best fit values were (in MHz)

$$C=-4283.84\pm0.01 ,$$

$$D=-28.06\pm0.06 ,$$

$$E=+7.10\pm0.02 .$$

The value of the reduced χ^2 for this fit is 1.37 (one degree of freedom).

The intersection of the planes is illustrated in Fig. 19 which is a section in the plane $E=+7.10$ MHz (the best-fit value), showing the error associated with each transition. The crossed bars show the best fit for the intersection and its associated errors in C and D.

For a pure $(1s,2p)$ configuration the ratio D/E would be[7] exactly -4. Our best fit gives $D/E=-3.950(10)$ in agreement with the theoretical value[7,20] $-3.945(11)$. A value of -4 would have given a very poor fit for the intersection of the planes, as is evident from Fig. 20 which shows C versus D with the constraint $D/E=-4$. Thus our results have given the first clear confirmation of this core-polarization effect.

D. Errors

The errors quoted in Sec. IV C for the hyperfine parameters were based on the uncertainties in D for each transi-

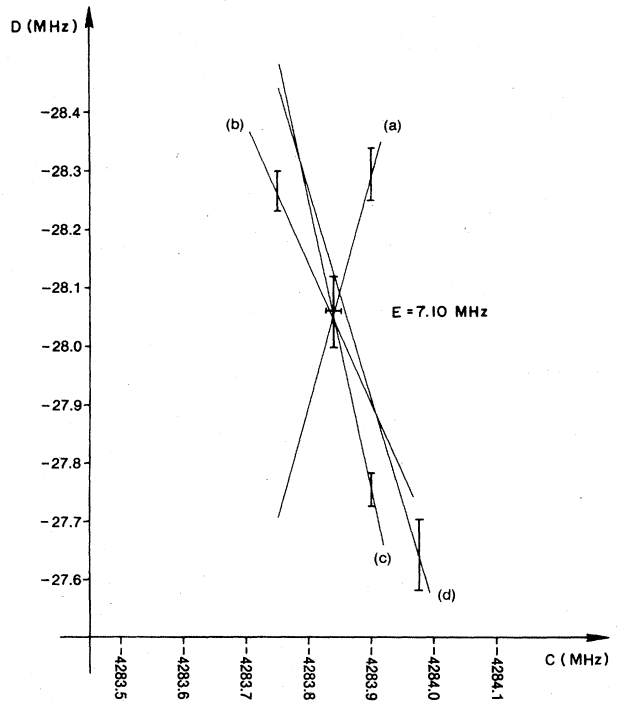

FIG. 19. Intersection of the transition planes shown as a plot of D vs C with E fixed at its best value of $+7.10$ MHz.

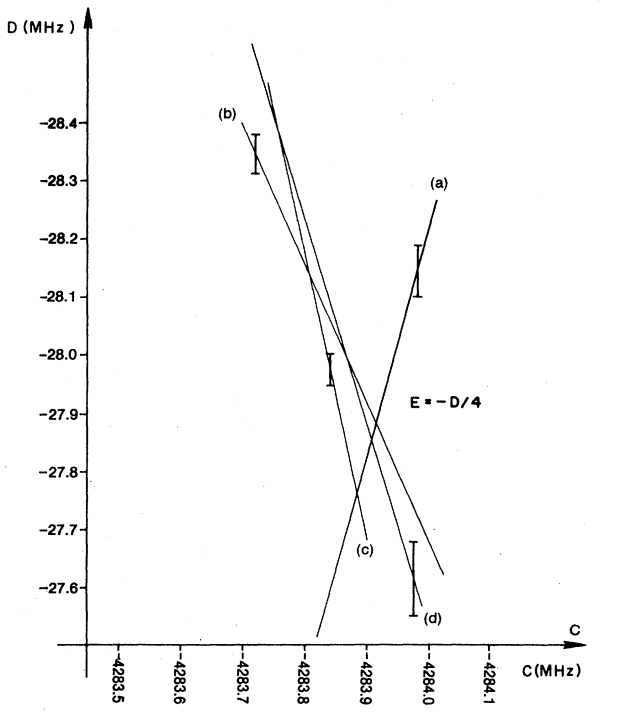

FIG. 20. Intersection of the transition planes for $D/E=-4$. The poor fit demonstrates the sensitivity of our data to core polarization.

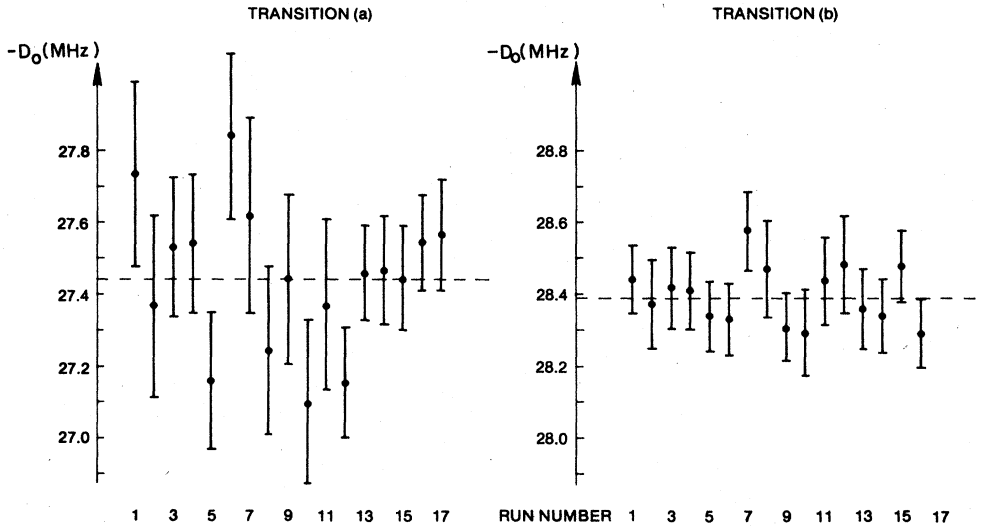

FIG. 21. Display showing the initial result D_0 of each run on transitions (a) and (b).

tion. These in turn resulted from statistical and field uncertainties. The statistical uncertainties were evaluated from the standard deviations for several measurements of the signal at each point in the line shape, and were found to be consistent with Poisson counting statistics. The field uncertainties were based on a 10-mG uncertainty in the absolute field measurement. In addition there was a correction for transition (d) due to the proximity, about 80 MHz or 16 linewidths away, of a $2\,^3S$ resonance. This correction produced a further uncertainty of 50 kHz in D for transition (d).

To be added to these were errors arising from uncertainties in the values of E_1, the $J=1$ to $J=2$ fine-structure separation, and C', the singlet-triplet hyperfine mixing parameter.[7] Errors due to uncertainties in the other parameters used in the data analysis were negligible. With the incorporation of these additional errors we obtained the following for our final values of the hyperfine parameters (in MHz):

$$C \equiv -4283.84^{+0.020}_{-0.010} ,$$

$$D = -28.06 \pm 0.06 ,$$

$$E = +7.10 \pm 0.02 .$$

Errors due to the Doppler effect and Bloch-Siegert and light shifts were negligible as discussed in Ref. 8.

Figure 21 summarizes the results of the individual experimental runs on transitions (a) and (b) for the preliminary fitting parameter D_0 defined in Sec. IV C. In each case the weighted mean is indicated by a dotted line. For all four transitions we found that the deviations of the individual runs from the mean were statistically consistent with the independently evaluated experimental errors, as is evident in the examples shown in Fig. 21. In addition we checked for extraneous field-dependent effects which would have produced systematic errors due to line-shape

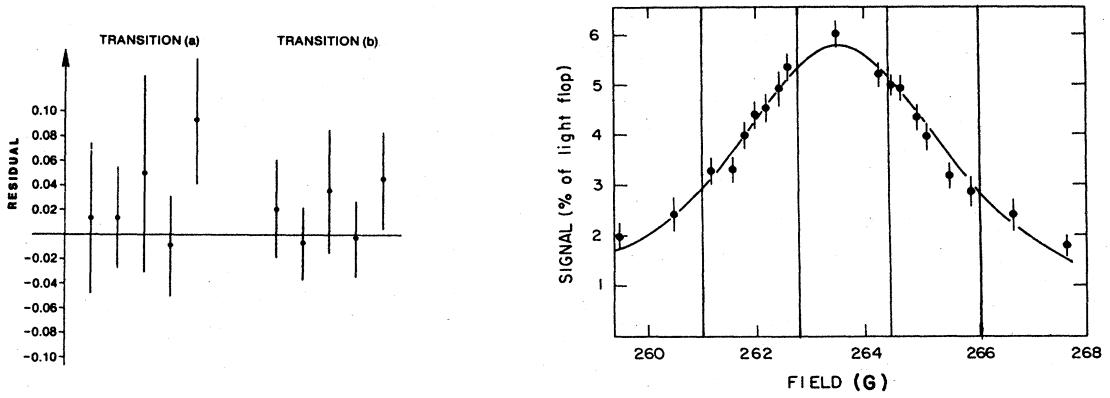

FIG. 22. Graph on the right shows how the resonance line was divided into five parts. Display on the left shows the average over all runs of the residuals in each part.

TABLE V. Summary of all precise experimental and theoretical results on the $2\,^3P$ state of ^{3}He. The theory is summarized in Ref. 7. ABMR denotes our atomic-beam magnetic resonance results.

Parameter	Experiment		Theory
	ABMR	Level crossing	
C	$-4283.84^{+0.02}_{-0.01}$ MHz[a]		$-4283.89(2)$ MHz
C'/C		1.010(16)[c]	$1.004^{+0.002}_{-0.01}$
D	$-28.060(60)$ MHz[a]	$-28.145(21)$[c]	$-28.128(8)$ MHz
D/E	$-3.950(10)$[a]	$-3.944\,5(21)$[c]	$-3.945(11)$
g_S'	2.002 243 2(22)[b]		2.002 239 9
g_L'	0.999 825 0(90)[b]	0.999 828 6(20)[c] 0.999 826 5(30)[d]	0.999 833 0(4)

[a]Present work.
[b]Reference 9.
[c]References 1 and 6.
[d]Reference 15.

asymmetries. This was done by dividing the line shape into five parts as shown on the right in Fig. 22. For each part we computed the residual, which is the algebraic sum of the deviations of all the experimental points from the fitted line shape. The results averaged over all runs are illustrated on the left in Fig. 22 for transitions (a) and (b). In all cases the residuals were statistically consistent with zero.

E. Discussion

In Table V our results are compared with theory and with those obtained from level-crossing measurements. We see all experiments are consistent with each other and with the theory, leading us to conclude that the hyperfine structure in the $2\,^3P$ state of ^{3}He is now well understood to the order of about 20 kHz in the interaction constants.

ACKNOWLEDGMENTS

This work was supported in part by the National Science Foundation. One of us (E.A.H.) was a recipient of support from the Alfred P. Sloan Foundation. Valuable discussions and encouragement came from Vernon Hughes of Yale University.

*Present address: Time and Frequency Division, National Bureau of Standards, Boulder, Colorado 80303.
†Present address: North Carolina State University, Raleigh, North Carolina 27650.

[1]K. R. German, Ph.D. thesis, University of Michigan, 1967; Bull. Am. Phys. Soc. **11**, 61 (1966).
[2]J. P. Descoubes, in *Physics of One- and Two-Electron Atoms,* edited by F. Bopp and H. Kleinpoppen (North-Holland, Amsterdam, 1969), p. 341; J. Derouard, M. Lombardi, and R. Jost, J. Phys. (Paris) **41**, 819 (1980).
[3]L. A. Bloomfield *et al.*, Phys. Rev. A **26**, 713 (1982); L. A. Bloomfield *et al.*, *ibid.* **26**, 3716 (1982); J. E. Lawler *et al.* Phys. Rev. Lett. **42**, 1046 (1979); F. Biraben *et al.*, J. Phys. B **13**, L685 (1980); D. Bloch, G. Trénec, and M. Leduc, *ibid.* **18**, 1093 (1985).
[4]R. R. Freeman *et al.*, Phys. Rev. A **22**, 1510 (1980).
[5]K. Tillman, H. J. Andrä, and W. Wittman, Phys. Rev. Lett. **30**, 155 (1973).
[6]E. A. Hinds, J. D. Prestage, and F. M. J. Pichanick, Phys. Rev. A (to be published).
[7]E. A. Hinds, J. D. Prestage, and F. M. J. Pichanick, this issue, Phys. Rev. A **32**, 2615 (1985).
[8]F. M. J. Pichanick, R. D. Swift, C. E. Johnson, and V. W. Hughes, Phys. Rev. **169**, 55 (1968).
[9]S. A. Lewis, F. M. J. Pichanick, and V. W. Hughes, Phys. Rev. A **2**, 86 (1970).
[10]A. Kponou, V. W. Hughes, C. E. Johnson, S. A. Lewis, and F. M. J. Pichanick, Phys. Rev. A **24**, 264 (1981).
[11]W. Frieze, E. A. Hinds, V. W. Hughes, and F. M. J. Pichanick, Phys. Rev. A **24**, 279 (1981).
[12]J. D. Prestage, E. A. Hinds, and F. M. J. Pichanick, Phys. Rev. Lett. **50**, 828 (1983).
[13]W. D. Phillips, W. E. Cooke, and D. Kleppner, Metrologia **13**, 179 (1977).
[14]W. L. Williams, Ph.D. thesis, Yale University, 1966.
[15]C. Lhuillier, J. P. Faroux, and N. Billy, J. Phys. (Paris) **37**, 335 (1976).
[16]M. L. Lewis and V. W. Hughes, Phys. Rev. A **11**, 383 (1975).
[17]S. D. Rosner and F. M. Pipkin, Phys. Rev. A **1**, 571 (1970).
[18]B. E. Zundell and V. W. Hughes, Phys. Lett. **59A**, 381 (1976).
[19]C. B. Lucas, Vacuum **23**, 395 (1972).
[20]W. Farr and E. W. Otten, Appl. Phys. **3**, 367 (1974).